Composites Part B 225 (2021) 109263

Contents lists available at ScienceDirect

Composites Part B

journal homepage: www.elsevier.com/locate/compositesb

Development of a curcumin-based antifouling and anticorrosion sustainable polybenzoxazine resin composite coating

Yajun Deng [a], Lixue Xia [b], Guang-Ling Song [a,c,d,*], Yan Zhao [b,e,**], Yanmei Zhang [f], Yuqing Xu [a], Dajiang Zheng [a]

[a] Center for Marine Materials Corrosion and Protection, College of Materials, Xiamen University, Fujian, Xiamen, 361000, China
[b] State Key Laboratory of Silicate Materials for Architectures, International School of Materials Science and Engineering, Wuhan University of Technology, Hubei, Wuhan, 430072, China
[c] State Key Laboratory of Physical Chemistry of Solid Surfaces, Xiamen University, People's Fujian, Xiamen, 361000, China
[d] The University of Queensland, St. Lucia, Qld, Australia
[e] The Institute of Technological Sciences, Wuhan University, Hubei, Wuhan, 430072, China
[f] College of Chemistry and Chemical Engineering, Xiamen University, Fujian, Xiamen, 361000, China

ARTICLE INFO

Keywords:
Curcumin
Bio-based benzoxazine
Sustainable copolymer
Coating designed model
Anti-corrosion and anti-fouling functionalities
Molecular dynamics (MD) simulations

ABSTRACT

Polybenzoxazine is an outstanding and highly promising resin for many advanced applications. This paper reports on a series of sustainable high-performance coatings made of benzoxazine monomer synthesized via the Mannich reaction of curcumin, 3-aminopropyltriethoxysilane and paraformaldehyde. This curcumin-based polybenzoxazine resin was experimentally demonstrated for the first time to be an effective barrier layer, which could evidently reduce the corrosion rate of the substrate metal, and significantly resist the fouling attachment. In addition, it was found that an increased content of PEG in the resin could further improve the antifouling performance of the coating. Molecular dynamics (MD) simulations suggested that a carefully selected density of PEG molecules in the polybenzoxazine framework could critically affect the hydration layer and the interaction energy. The benzoxazine monomer and polymer were characterized by Fourier transform infrared (FT-IR), X-ray photoelectron spectroscopy (XPS), proton nuclear magnetic resonance (^{1}H NMR and ^{13}C NMR) spectroscopy, different scanning calorimetry (DSC), and thermogravimetric technique. The anticorrosion and antifouling of the developed polybenzoxazine resins were evaluated by potentiodynamic polarization, electrochemical impedance spectroscopy (EIS) and attachment of protein, bacteria and microalgae. The results showed that the polybenzoxazine coatings (PCB or PCBG-X) performed excellently in anticorrosion even after long-term exposure in corrosive environments, and some of the polybenzoxazine coatings, like PCBG-10 and PCBG-15, possessed a superior antifouling capacity. To simultaneously enhance the anticorrosion and antifouling, a double layer coating system was designed using the PCB resin as the sub-layer and the PCBG-10 or PCBG-15 film as the up-layer. The great long-term corrosion resistance of the coatings was confirmed by electrochemical measurements in salt immersion and salt-spray. It is expected that this new design of the promising polybenzoxazine resin coating system will find wide applications in marine industry and relevant fields.

1. Introduction

Metal is widespread material applied in every aspect such as architecture, medicine, transportation. The metal surface is often protected by a painting. In some environments, coatings with some special functions may also be applied for anti-corrosion, anti-biofilm attachment, anti-icing, anti-fogging or other purposes to enhance safety and reduce potential economic lose. Thermosetting resins are the important players in polymer science and the advanced material components used in protective barriers due to their high modulus, durability, stable thermal and chemical resistances in the civil infrastructures and transportation industries [1]. As a new and promising class of high-performance

* Corresponding author. Center for Marine Materials Corrosion and Protection, College of Materials, Xiamen University, Fujian, Xiamen, 361000, China.
** Corresponding author. State Key Laboratory of Silicate Materials for Architectures, International School of Materials Science and Engineering, Wuhan University of Technology, Hubei, Wuhan, 430072, China.
E-mail addresses: Guangling.song@hotmail.com, glsong@xmu.edu.cn (G.-L. Song), yan2000@whut.edu.cn (Y. Zhao).

https://doi.org/10.1016/j.compositesb.2021.109263
Received 25 June 2021; Received in revised form 26 August 2021; Accepted 27 August 2021
Available online 1 September 2021

thermosetting resin, polybenzoxazine resin is polymerized by the benzoxazine monomers via thermally activated ring-opening reaction without any catalysts and byproducts [2]. The benzoxazine monomer is synthesized by the Mannich condensation from phenol or phenol derivative, formaldehyde, and primary amine, thus the materials can provide high molecular design flexibility and unique stereochemistry to exhibit excellent capacities, such as nearly zero shrinkage upon curing, good mechanical properties, superior chemical and electrical resistances, and low water absorption, and to meet the various requirements and versatilities in the electronics, composites, aerospace, coatings, and many other fields [3,4]. Nevertheless, benzoxazine is facing the lack of raw materials from the petrochemistry resources, and the pressure of increasing cost, toxic waste, and environmental pollution [5]. For long-term sustainable and low-cost production using natural or recyclable resources, renewable raw materials, such as the alternative phenolic and/or amine derivatives, have become particularly favorable in polymerization of the partially or fully bio-based benzoxazines [6–8]. For example, eugenol is a natural phenol extracted from clove, which can be made into eugenol-based benzoxazines to improve the cross-linking density and thermal stability [9–11]. Chavicol can be extracted from bay oil, betel oil or sweet basil. A bio-based chavicol benzoxazine has been developed with crosslink ability that can be thermally activated [12,13]. Vanillin, which can be manufactured from lignin or other renewable materials, can react with benzoxazine to modify the thermal behavior [14,15]. Additionally, there are many other natural resources for phenol, such as urushiol [16], cardanol [17,18], resveratrol [6], guaiacol [19], cinnamic/cinnamates [20], coumarin [21,22], etc. The sustainable and ecofriendly benzoxazines, opted from the abundant and natural resources as reactant alternatives for synthetic monomers, have been developed into promising raw materials.

Curcumin, also known as 1,7-bis-(4-hydroxy-3-methoxyphenyl)-1,6-heptadiene-3,5-dione, is a yellow polyphenolic compound that can be extracted from rhizomes of turmeric. Curcumin possesses a pharmacological activity potentially and excellent therapeutic efficacy due to its bio-chemical functions, such as antioxidant, antibacterial, antiviral, anti-inflammatory, antiproliferative [23–26]. Besides, curcumin allows for high-performance of polymer synthesis because of the functional phenolic compound. To best of our knowledge, current investigations so far have never taken curcumin as a phenolic resource to synthesize benzoxazine. It is expected that the introduction of curcumin as a benzoxazine chemical feedstock can enhance the sustainability, antibacterial and/or antiviral activities, physical and chemical resistance, and anticorrosion property of the resins [3,4,24].

To inherit other functionalities of benzoxazine and expand its applications, incorporation of the chemical moieties or polymer chains of benzoxazine units is a favorable approach. For example, different natural and/or non-natural amino acids and renewable phenols have been utilized to fabricate polybenzoxazine poly-(E-lyme), which can act as a precursor in porous materials for CO_2 adsorption [2]. Patil et al. reported an amine functional benzoxazine resin, which was synthesized from cardanol, N, N′-bis(2-aminoethy-l)ethane-1,2-diamine and paraformaldehyde. The benzoxazine resin was utilized to modify the structure of 3-glycidoxypropyltrimethoxysilane (GPTMS) to improve the crosslinked framework for better barrier protection to corrosive species [27]. Poly(ethylene glycol) (PEG) can act as a functional polymer and/or modification agent to enhance the surface resistance to antimicrobial attachment and settlement [28–30]. By creating a hydration layer between water molecules and PEG chains, or by the “steric repulsion” of the chains, PEG or PEG-based copolymers possess well-established anti-biofouling activities against proteins, bacteria, cells, and other organisms [31]. The PDA-PEG coatings were fabricated with the polydopamine (PDA) and polyethylene glycol (PEG) as a bio-adhesive and antifouling agent to greatly reduce biofouling attachment on various substrates [32]. Random poly(HEMA-*co*-PEG_{10}MA) copolymer brushes grafted on a surface were prepared to study the relationship between hydration capacity and polymeric grafting density [33]. It was proposed that a too low and high polymeric density could reduce the antifouling capacity due to a low hydration layer formed. In an optimum thickness range, the polymers could exhibit effective antifouling property with strong hydration capacity and without entanglement or crowding effect of thick polymeric chains.

To produce an ecologically ecofriendly “green” coating, nontoxic natural precursors are basically used instead of other booster biocides. Thus, in the present work, a bio-based high-performance benzoxazine was synthesized sustainably using curcumin, 3-aminopropyltriethoxysilane and paraformaldehyde as raw materials. Different loadings of hydrophilic PEG molecules in the monomer were incorporated in the synthesized benzoxazine to acquire the resin inherent properties and enhance its anti-biofouling performance via modification of resin framework. These designed coatings prepared from these chemical materials are based on the following considerations: i) Curcumin, as a natural and renewable phenol, contains inherent functionalities; ii) Curcumin molecule containing two phenolic hydroxyl groups can improve the cross-link density if the bioactive bisbenzoxazine resin. iii) 3-aminopropyltriethoxysilane (APTES) is used as the common and low-cost amine source, and the Si–O–Si framework can improve the resin crosslinking after polymerization. vi) The as-prepared coatings have low water absorption, as well as antifouling and anticorrosion capacities. v) Without booster biocides, the resins perform excellent repellent property due to the beneficial effect of a certain content of PEG. The purpose of this work, therefore, was to characterize the synthesis and structure of the curcumin-based benzoxazine monomer and its co-reaction with PEG by means of Fourier transform infrared spectroscopy (FT-IR), X-ray photoelectron spectroscopy (XPS) and nuclear magnetic resonance spectroscopy (^{1}H NMR and ^{13}C NMR). The thermal stability of the coatings was studied by thermogravimetric analysis (TG) and different scanning calorimetry (DSC). Upon fabrication of functional polybenzoxazine resin (PCB or PCBG-X), the antifouling properties in resisting protein, bacteria and microalgae adsorption were systematically evaluated. To understand the resisting effect, an anti-adhesive mechanism was elucidated by molecular dynamics (MD) simulations, as it was hard to be detected by experiment. The results showed that a certain content of PEG critically determined the fouling repellency due to a strong hydrated layer and interaction energy of the coating surface. Besides, the anticorrosive behavior of the coatings (PCB or PCBG-X) was monitored by electrochemical impedance spectroscopy and evaluated by potentiodynamic polarization, and their corrosion morphologies were observed at different periods. More importantly, a coating system model was proposed with the PCB as the anti-corrosion sub-layer and the PCBG-10 or PCBG-15 as the antifouling up-layer to synergistically perform the excellent multi-functionalities.

2. Results and discussion

2.1. Synthesis and structural characterization of CB, PCB and PCBG

Benzoxazine monomer, CB, was synthesized via Mannich condensation from renewable curcumin, 3-aminopropyltriethoxysilane and paraformaldehyde to form the oxazine ring, as shown in Scheme 1. On the basis of the relevant literatures [34–40], the probable polymerization mechanism of CB process was thermally mediated at the ring-opening polymerization (ROP) temperature as detailed in Scheme 2. Via the cleavage of O–CH_2–N in the oxazine ring, the cationic moieties of zwitterionic intermediates were formed. The adjacent benzoxazine monomers attacked the cationic imine moieties though electrophilic substitution. Consequently, the structure was rearranged to form a new type of Mannich bridge. Furthermore, the triethoxysilane groups of the benzoxazine monomers were catalyzed by hydrochloric acid to form Si–OH groups. The Si–OH groups would convert into the Si–O–Si linkages to cooperate with the Mannich bridge portion to reinforce the polybenzoxazine cross-linking framework.

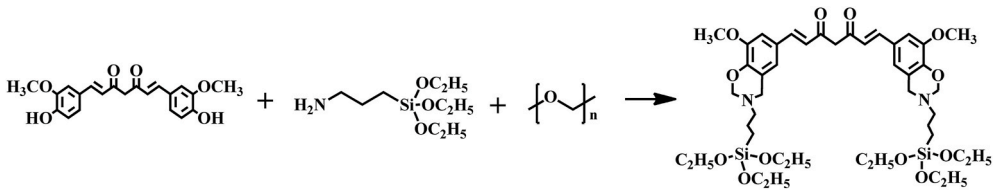

Scheme 1. Synthesis reaction of the curcumin-based benzoxazine monomer (CB).

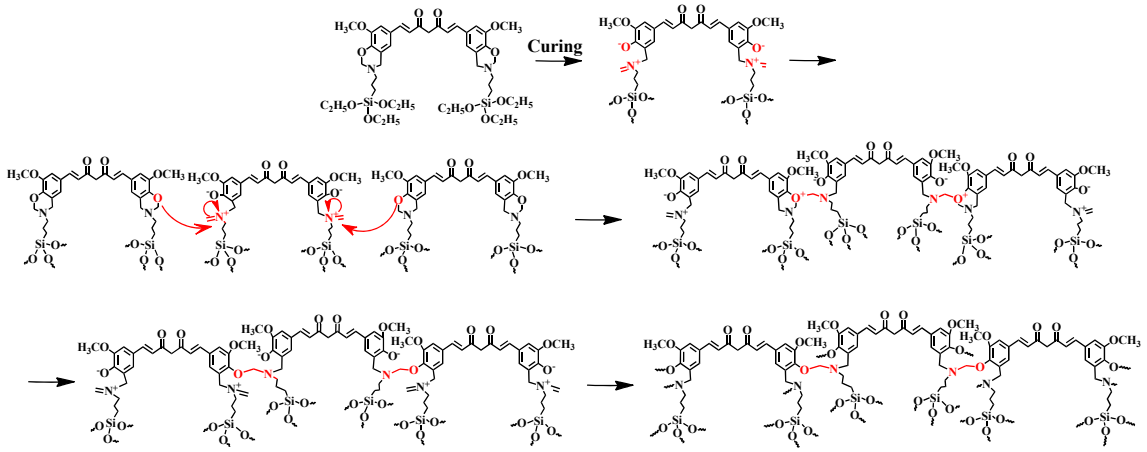

Scheme 2. Thermal induced ring-opening polymerization of functional curcumin-based benzoxazine.

The chemical structure of the monomer CB was examined by ^{1}H NMR, ^{13}C NMR, FTIR, and XPS spectroscopy. The ^{1}H NMR and ^{13}C NMR results are presented in Fig. S1. The characteristic proton resonances at 3.90 and 4.96 ppm were assigned to the Ar-CH_2-N (g) and O–CH_2–N (f) of benzoxazine groups, respectively. The signals at 1.14 and 3.73 ppm were attributed to –CH_3 (l) and –OCH_2 (k) of triethoxysilane groups, respectively. The peak at 3.82 ppm was assigned to the characteristic group of –OCH_3 (a). The ^{13}C NMR spectra of benzoxazine monomer CB showed the resonances at ~7.41 ppm (-Si**C**H_2CH_2), ~18.12 ppm (-OCH_2**C**H_3), ~21.26 ppm (-CH_2**C**H_2CH_2), ~53.89 ppm (-N**C**H_2C), ~58.15 ppm (-O**C**H_2CH_3) and ~83.06 ppm (N–**C**H_2–O). As shown in Fig. 1 (a), the CB characteristic absorption band at 1382 cm^{-1} in FTIR spectrum corresponded to a –CH_2 stretching vibration wagged in benzoxazine rings. The stretching vibration of C–O–C at 1276 cm^{-1} and the out-of-plane bending of C–H at 955 cm^{-1} were detected from the obtained benzoxazine precursor [41]. The typical adsorption peak at 1516 cm^{-1} was from the vibration of aromatic C=C [42]. Meanwhile, the adsorption of benzoxazine ring (955 cm^{-1}) and asymmetric stretching of Si–O–C (1078 cm^{-1}) disappeared, and the vibration peak simultaneously appeared at 1108 cm^{-1}, which was interpreted as the Si–O–Si formation after curing [39,43]. Those results confirmed the successful formation of monomer and polybenzoxazine. The XPS analysis of CB

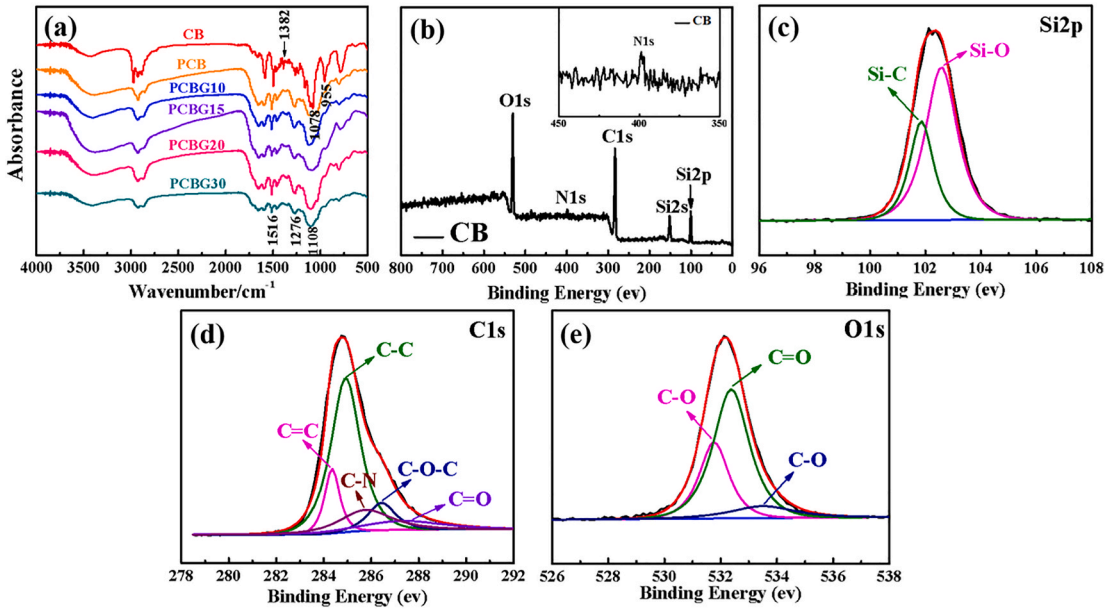

Fig. 1. (a) The FT-IR absorbance spectra of CB monomer and different polymers, (b) the XPS analysis of the benzoxazine monomer CB and the CB elements of Si (c), C (d), O (e).

monomer elements is presented in Fig. 1(b–e). The four elements of CB monomer were identified as Si, C, O and N. Especially, the high-resolution Si 2p spectrum peaks at 101.8 and 102.5 eV indicated the formation of C–Si and Si–O groups (Fig. 1 (c)) [44]. As shown in Fig. 1 (d), the high-resolution C1s spectrum could be fitted into five peaks at 284.3, 284.9, 285.7, 286.4 and 287.6 eV, and it indicated the existence of C═C, C–C, C–N, C–O–C and C═O bonds, respectively [45–47]. The O 1s spectrum peaks at 531.7 and 533.5 eV presented C–O bond, whereas the peak at 532.3 eV demonstrated the formation of C═O bond [45,48]. Thus, these characteristic results illustrated that both of the successfully fabricated monomer CB and polybenzoxazine contained desirable groups.

The purity of the CB monomer was further indicated by the content of free amine groups using ninhydrin assay (Fig. S2). The reaction of CB with ninhydrin resulted in a green colored compound, while the reaction of APTES with ninhydrin presented a purple colored compound. The purple compound was identified by the maximum absorbance at 560–570 nm in the UV–vis spectrum, while it was absent in the CB monomer, confirming the absence of APTES impurity [41,49]. Besides, the element analysis of the monomer is shown in Table S1. The C, H and N element contents were respectively 56.58, 7.68 and 3.62 wt%. The experimental results were similar to the theoretical values, suggesting that the CB had a high purity.

The thermogravimetric analysis (TGA), differential thermogravimetric analysis (DTA) and differential scanning calorimetry (DSC) curves of the monomer CB are presented in Fig. 2(a–b). The $T_{5\%}$ (5% mass loss temperature) and $T_{10\%}$ (10% mass loss temperature) of the monomer were at 175.81 and 207.81 °C, respectively. The maximum derivative peak at 418.81 °C was due to the Mannich bridge cleavage [39]. As shown in Fig. 2 (b), an endothermic peak appeared at 165.23 °C due to the ring-opening polymerization. At a higher temperature around 300.83 °C, the triethoxysilyl groups underwent a further condensation process, resulting in formation of siloxane linkages [50]. After that, CB monomer had a higher broad temperature range on the exotherm peak which started at 314.50 °C and reached the maximum at 372.83 °C. The TGA and DTA curves in the nitrogen atmosphere shown in Fig. 2(c–d) indicated the thermal stabilities of the different coatings. The corresponding gravimetric analysis data of the monomer CB and the cured coatings are summarized in Table S2. In the degradation stage <200 °C, the thermal scission of PEG main chain of the coating occurred [51,52]. As indicated by $T_{5\%}$ and $T_{10\%}$, the initial thermal stability of PCB was higher than the others with different contents of PEG. For example, the $T_{5\%}$ (286.83 °C) and $T_{10\%}$ (330.83 °C) of PCB were higher than those of the PCBG coatings. The TGA and DTA curves confirmed that all the resins were thermally stable up to about 390 °C, and in the range from 399.32 to 411.83 °C, all the coatings showed the maximal thermal degradation due to Mannich bridge cleavage. To further analyze the thermal characteristics of the different coatings, the char yields of all the curing resins PCB, PCBG-10, PCBG-15, PCBG-20 and PCBG-30 at 800 °C were respectively 59.64. 48.84, 47.88, 47.66, 44.18%, revealing that all the polybenzoxazines had good thermal stability at the range from 25 to 800 °C.

Furthermore, the mechanical properties of the composite coatings, including the coating hardness, adhesive strength and abrasion consumption, were measured, and the results are shown in Fig. S3 and Table S3. The adhesion strength decreased at a higher content of PEG in the polybenzoxazine framework (see in Table S3). This could be interpreted by the fact that increased content of PEG chains combine with the Si–O bonds and reduce the Si–O–Fe bonds. The latter should be responsible for the adhesion of the coating with the substrate steel. The dependence of the coating mass loss on the abrasion cycle is presented in Fig. S3 (a), and the microscopic images of the different coatings before and after abrasion are shown in Fig. S3 (b). The glossiness of all the coatings had a similar descend tendency in the first 25 abrasion cycles, and after that there was no obvious difference in glossiness. These indicated that the abrasion and hardness of the coatings were inversely related. Meanwhile, the coating mass decreased slightly with the increasing abrasion cycles even after 50 cycles, indicating that all the coatings had good mechanical abrasion resistance. This high abrasion resistance could be attributed to the outstanding crosslinking framework

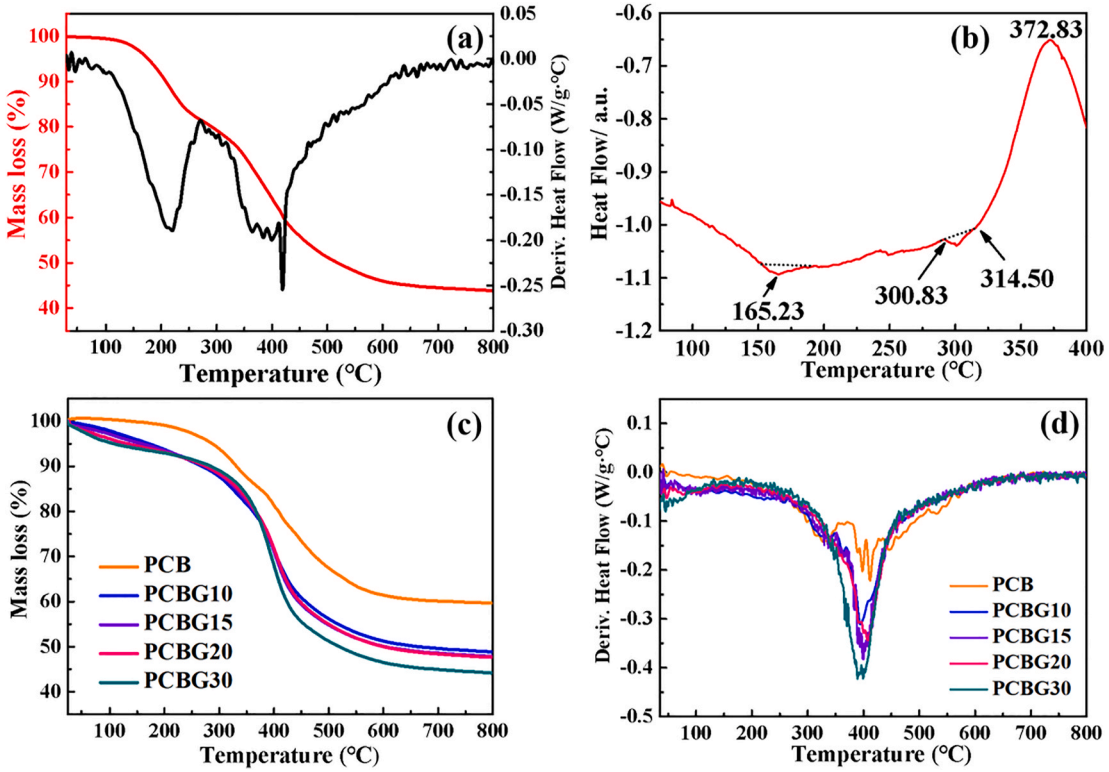

Fig. 2. (a) TGA thermograms and DTA traces of CB monomer, (b) DSC curve of CB monomer, (c) TGA thermograms and (d) DTA traces of different coatings.

in the coatings.

2.2. Antifouling property of PCB and composite PCBG resins

It is an important strategy to create an intrinsic antifouling surface with a foulant-repelling ability to reduce protein or bacterial attachment at the initial stage. Protein adsorption is the first step in the primary biofilm formation and it promotes other organism attachment as it can alter the surface physicochemical properties. Afterwards, bacterial settlement on the surface is facilitated leading to the sequent colonization. Hence, the anti-adsorption of protein on a coating critically determines the antifouling performance of the coating. In this study, to measure the protein anti-adsorption on the different coatings, bovine serum albumin labelled by the fluorescein isothiocyanate (BSA-FTIC) was used as the fouling specie to detect the antifouling ability of the different coatings. The fluorescence microscopic images of the BSA-FTIC on the pristine glass and coating surfaces are shown in Fig. S4. The quantity of the adhered BSA-FTIC on the coating surfaces obviously decreased, showing that the fluorescence intensity values of the different coatings significantly reduced relative to that of bare glass (1.04 ± 0.02) (Fig. 3 (a)). Thus, all the coatings exhibited anti-adsorption efficiencies in the range from 51.17 ± 1.28% to 90.82 ± 0.71%. Two of the coatings PCBG-10 and PCBG-15 possessed higher efficiencies at 90.82 ± 0.71% and 86.13 ± 1.77%, respectively, than the bare glass (Fig. 3 (b)). To assess the antibacterial activities of the coatings against *E. coli* and *S. aureus*, the adhered bacteria in the LB medium were incubated. The fluorescence microscopic images of *E. coli* and *S. aureus* bacteria with higher intensities (5.93 ± 0.03 and 15.42 ± 0.01, respectively) as shown in Fig. 4 (b) indicated that large amounts of the two bacteria were attached on the pristine glass (Fig. 4 (a) and Fig. S5). By direct visual comparison with the pristine glass images, the polybenzoxazine coatings showed effectively inhibited bacterial attachment. Those results suggested that all the coatings were highly efficient against the bacterial adhesion (see Fig. 4 (c)). Meanwhile, the attached bacteria *E. coli* and *S. aureus* on the pristine glass and coating surfaces were observed via SEM as shown in Fig. 4 (d). There were plenty of aggregated bacteria *E. coli* or *S. aureus* attached on the pristine glass, while a small amount of bacteria adhered on the coating surfaces, which exhibited the higher anti-attachment efficiencies of the coatings for bacteria *E. coli* and *S. aureus*, especially the PCBG-10 (95.09% ± 0.14 and 91.25% ± 0.06, respectively) and PCBG-15 (93.06 ± 0.04 and 93.65 ± 0.20, respectively).

Microalgae are the unwanted colonization on an artificial surface in some marine environments because they can easily settle on a wide range of surfaces after the adsorbed proteins and bacteria have formed a marine conditioning biofilm. The biofouling colonization on an immersed substrate can also cause significant corrosion and potentially hazard a structure in service. Thus, microalga can be used as a model fouling specie to evaluate the coating antifouling behavior. The settlement image, average fluorescence intensity and efficiency of microalgae *N. closterium* and *Dicrateria zhanjiangensis* on the coatings are presented in Fig. 5 (a), Fig. S6 and Fig. 5 (b and c). For the pristine glass, the uniformly brilliant fluorescence intensity indicated that a large amount of microalgae had been equably absorbed on the surface. Fortunately, the coverages of the microalgae on the PCB coating decreased and showed anti-fouling efficiencies at 40.81% and 38.73% compared with the pristine glass (see Fig. 5 (c)), respectively. The PCBG coatings showed the decreased fluorescence intensities and high fluorescence efficiencies relative to the pristine glass, especially the coatings PCBG-10 (70.59% ± 0.02 and 76.09% ± 0.01, respectively) and PCBG-15 (75.59% ± 0.03 and 80.27% ± 0.01, respectively). In contrast to the small amounts of the microalgae on the coatings PCBG-10 and PCBG-15, the fluorescence intensities of the coatings PCBG-20 and PCBG-30 noticeably increased. These microalgae attachment results were similar to the adsorption behaviors of the BSA-FTIC, *E. coli* and *S. aureus* bacteria on the coatings.

The superb antifouling performance of the coatings confirms the effect of the curcumin ingredient and the additional PEG segment in the polybenzoxazine. As illustrated in Fig. 6(a–b), the curcumin is deemed to play the inherent antifouling role in the framework of the polybenzoxazine coatings. In addition, except the open rings in the benzoxazine to form polymeric crosslinking, the Si–O–Si groups are the important framework in the structure, and they can impact the coating antifouling properties (Fig. 6(a–b)). Surface free energy is a vital factor influencing the biofouling and bio-adhesive activity of a coating. Some reports have illustrated that the minima bacterial adhesion occurs on films with surface free energy around 20–30 mJ/m^2 [53–55]. The surface free energies of different coatings were determined by contact angles of deioinized water, ethylene glycol and diiodomethane, and the van Oss and Good's three-liquid method was used to calculate the energies. As shown in Table S4, the surface free energies of the coatings fell in the range of 25.62–34.06 mJ/m^2. The PCB coating exhibited relatively low surface free energy which might be one of reasons that the PCB had the anti-adhesion capacity. The variation of surface energy with the increasing content PEG in the coating was relatively small. It was interesting that the PCBG-10 and PCBG-15 with surface free energies around the middle values (30.09 and 30.76 mJ/m^2) demonstrated their best anti-biofouling activities. In this case, the surface free energy was not the only parameter determining the anti-adhesion of the coating against organisms, and other factors could also effectively influence the fouling repellency [33].

PEG is an effective fouling-resistant functional polymer chain in a system. The hydrophilic PEG in a coating structure can interact with water molecules, stretch in the aqueous environment, and possess the strong hydration layer [56]. Thus, the electrostatic and hydrophilic interactions between the surface and bacteria can be blocked by the hydration layer, which will efficiently repel protein or bacterial attachment [57]. Furthermore, the chain length and density of PEG molecule in the polymer conformation are two of the key factors

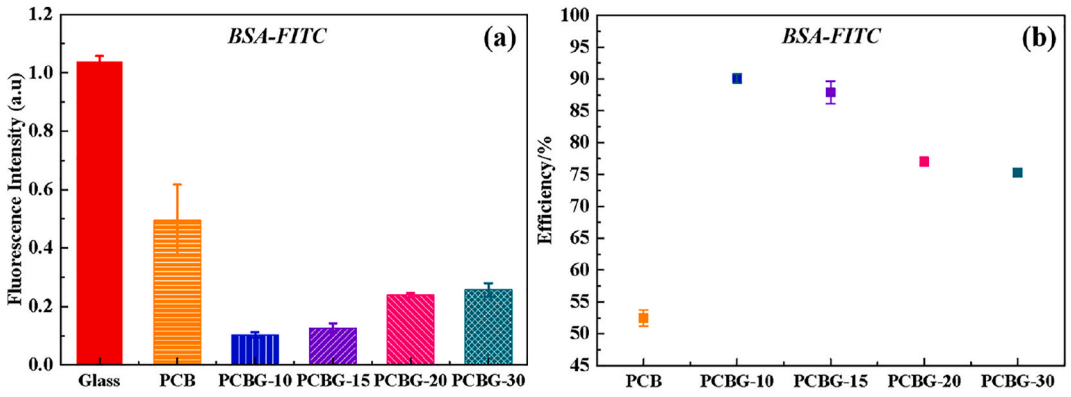

Fig. 3. (a) Fluorescence intensity and (b) anti-adsorption efficiency of different surfaces after protein adsorption test.

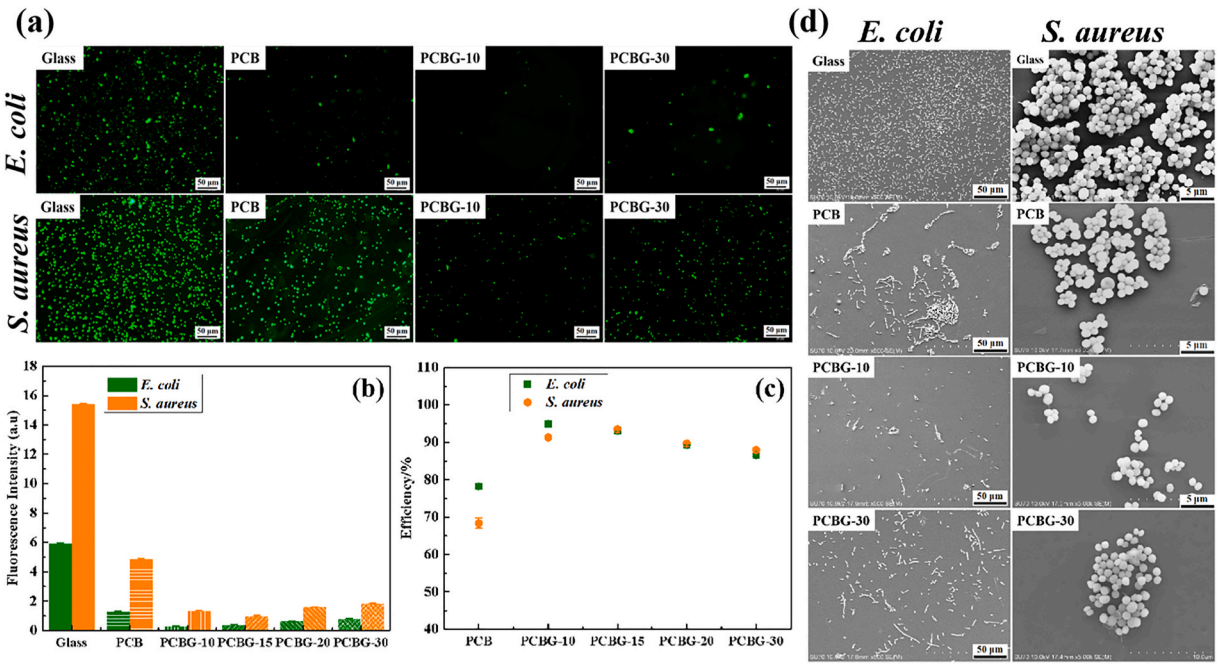

Fig. 4. (a) Fluorescence microscopic images of bacteria *E. coli* and *S. aureus* settled on different surfaces after 6 h of immersion in bacterial suspensions, (b) fluorescence intensity, (c) efficiencies, and (d) microcosmic images of bacteria *E. coli* and *S. aureus* settled on different surfaces.

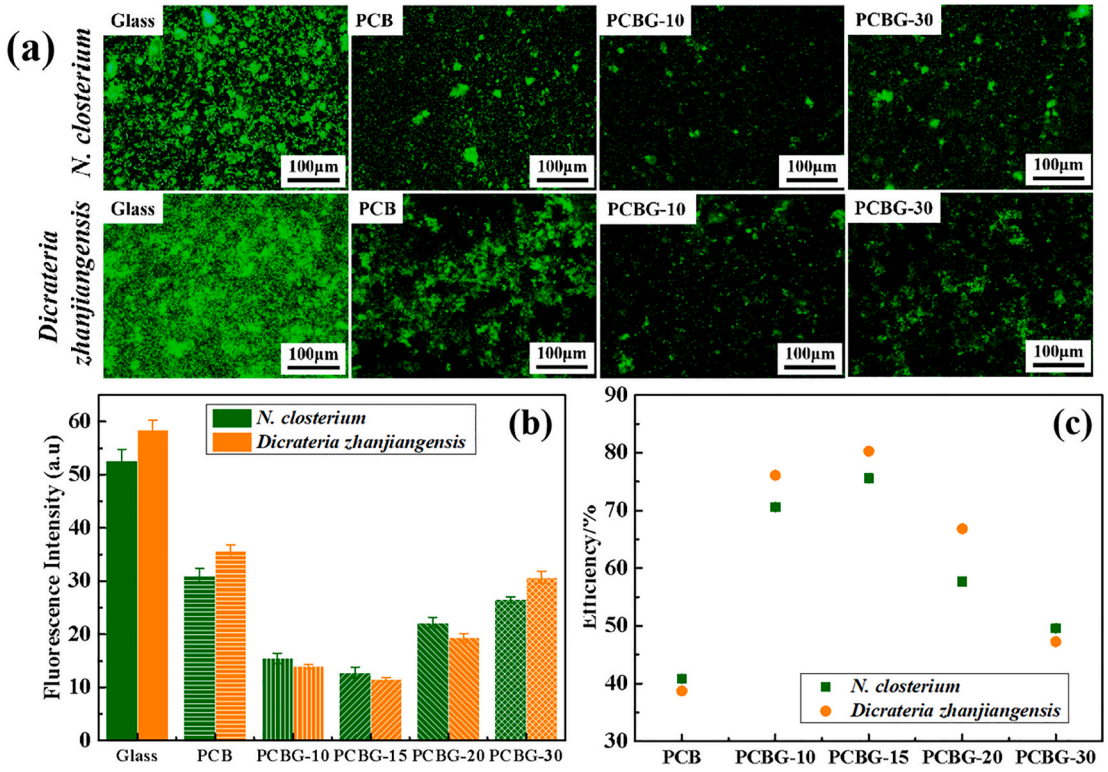

Fig. 5. (a) Fluorescence microscopic images of microalgae *N. closterium* and *Dicrateria zhanjiangensis* settled on different surfaces after 7 days of immersion in microalgae medium, (b) fluorescence intensities, and (c) efficiency of microalgae *N. closterium* and *Dicrateria zhanjiangensis* settled on different surface.

affecting the antifouling performance [31]. Some reports have revealed that the low molecular weight of PEG coatings show optimal antifouling ability to minimize the attachment of foulants, because of the steric repulsion effect [31,58–60]. Therefore, the low molecular weight PEG chain with M_n = 800 was chosen in this work. Besides, some reports suggested that the density rather than the chain length was more important for antifouling efficiency [61,62]. For example, via grafting different chain densities to form different polymeric thickness, the effect of the random poly(HEMA-*co*-$PEG_{10}MA$) chain density and thickness on anti-attachment behavior was studied profoundly [33]. It was concluded that a higher PEG chain density could cause a negative entanglement or crowding effect, leading to a weak hydration layer which could seriously

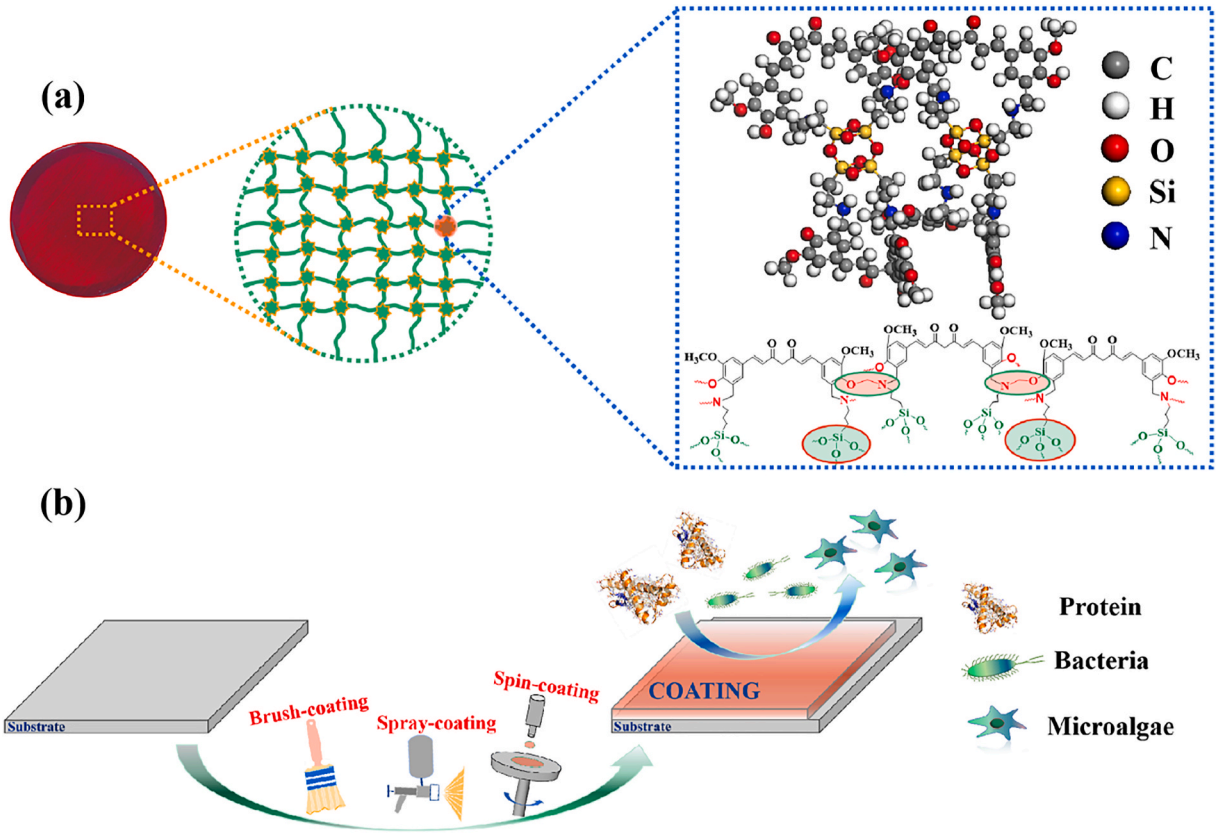

Fig. 6. (a) Schematic molecular structure and crosslinking interaction of PCB coating, and (b) schematic illustration of the coating-forming method and antifouling property against protein, bacteria, and microalgae.

affect the antifouling performance.

However, the hydration layer can not be directly revealed via coating experiments at the molecular level theories. In this study, the hydration layer and the coating interaction energy effect were elucidated by the molecular dynamics (MD) simulation to understand the varied anti-attachment of fouling on the coatings with different PEG densities. Since the composition and structure of the three-dimension configuration of the PEG and PCB are extremely complicated, a simplified model of those materials was taken to construct the simulation system, as shown in Fig. S7. Lipophilic benzene molecule (used as a typical fouling compound) [63] was introduced into the coating surface (PCBG-10 or PCBG-30) without or with water media from the MD simulations system, and their average interaction energy was calculated (see Fig. 7(a–c)). When benzene molecules entered the PCBG-10 coating in the absence of water, the calculated surface interaction energy reached −11.5166 kcal/mol, indicating that all the benzene molecules could be easily attached on the coating surface because of their strong interaction (see Fig. 7 (a), and Movie 1, ESI). In contrast, when the average calculated interaction energy between benzene molecules and PCBG-10 coating reached higher energy at −8.3128 kcal/mol, the benzene could not be firmed adsorbed on the coating, In this case, if water molecules were mixed into the simulation system (see Fig. 7 (b)), they would form a hydration layer due to the stable interaction between the water and coating polymers. Much less lipophilic benzene molecules were unstably adsorbed on the surface, because benzene molecules were difficult to surpass the dissociation higher energy barrier of the water molecules to reach coating surface. Even if there were few, they could be easily repelled away from the surface (see Fig. 7 (b), and Movie 2, ESI). While adding an increased PEG content into the coating, the average interaction energy between the benzene and coating PCBG-30 reached −10.9623 kcal/mol. The more lipophilic benzene molecules could lead to stronger covalent and/or hydrogen bond with the hydration layer and polymeric chains. Thus, they were more easily adsorbed on the PCBG-30 surface than on the PCBG-10 (see Fig. 7 (c), and Movie 3, ESI). Both the simulation and experiments indicated that the fouling repellent performance of the coatings obviously reduced with increasing PEG content in the coating due to the low interaction energy and the formation of a hydration layer.

Supplementary video related to this article can be found at http s://doi.org/10.1016/j.compositesb.2021.109263.

2.3. Anticorrosion property of PCB and composite PCBG resins

Biofouling is defined as undesirable adhesion and accumulation of micro- and macro-organisms on a surface after immersion in aqueous environments. After micro-organisms aggregate, form a biofilms, and grow into organic fouling firmly attached on a metal surface, the corrosion, more specifically the microbially influenced or induced corrosion (MIC), can be initiated and accelerated electrochemically by the microorganisms [64,65]. Therefore, the coating is the important layer to act as a barrier to hinder or minimize the chemical or electrochemical process between the metal and fouling. To meet the demands for antifouling and anticorrosion performance and reduce the cost, many multifunctional coatings have been developed, which has currently become a hot topic in the coating industry.

To investigate the anticorrosive performance, potentiodynamic polarization curves of bare steel and different polybenzoxazine coatings (23 ± 3 μm) were analyzed as shown in Fig. 8. The corresponding electrochemical parameters including corrosion potential (E_{corr}), apparent corrosion current density (I_{corr}) and protection efficiency (PE) were shown in Table 1. The corrosion potentials and corrosion current densities of different coatings were obtained by the Tafel extrapolation method. The protection efficiency (PE) is calculated by Eq. (1).

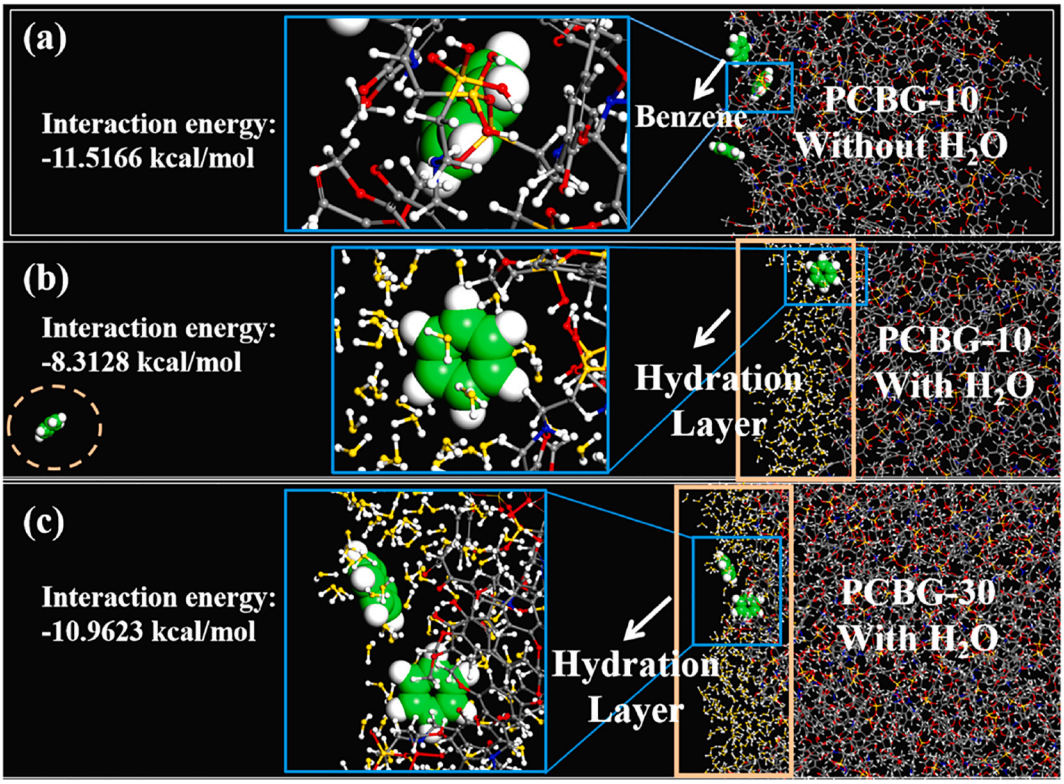

Fig. 7. (a) Benzene-PCBG-10 without H_2O, (b) benzene-PCBG-10 with H_2O and (c) benzene-PCBG-30 with H_2O after MD simulation (yellow, H atoms of H_2O, white, O atoms of H_2O; white, H atoms of benzene, green, C atoms of benzene; gray, C atoms of PCBG-10 and PCBG-30; white, H atoms of PCBG-10 and PCBG-30; red, O atoms of PCBG-10 and PCBG-30; blue, N atoms of PCBG-10 and PCBG-30; yellow, Si atoms of PCBG-10 and PCBG-30). (For interpretation of the references to color in this figure legend, the reader is referred to the Web version of this article.)

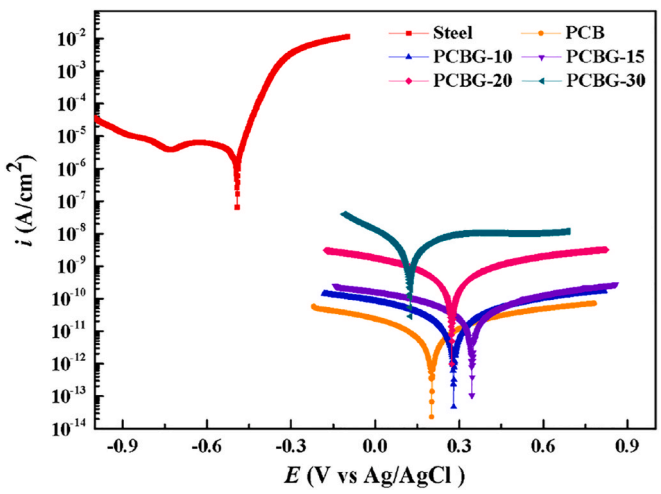

Fig. 8. Potentiodynamic polarization curves for bare steel and different coatings in 3.5 wt% NaCl solution.

Table 1
Electrochemical parameters extracted from the polarization curves.

Sample	E_{corr} (V vs Ag/AgCl)	I_{corr} (μA/cm^2)	Protection Efficiency (%)
Bare Steel	−0.049	4.721	–
PCB	0.201	3.864×10^{-6}	99.9999
PCBG-10	0.279	2.815×10^{-5}	99.9994
PCBG-15	0.345	5.546×10^{-5}	99.9988
PCBG-20	0.270	5.464×10^{-4}	99.9884
PCBG-30	0.125	3.456×10^{-3}	99.9268

$$PE = \frac{I_{corr,bare} - I_{corr,coated}}{I_{corr,bare}} \times 100\% \quad (1)$$

where $I_{corr,\ bare}$ and $I_{corr,\ coated}$ refer to the corrosion current density of the bare steel and the coating, respectively.

As shown in Table 1, the I_{corr} of bare steel was 4.721 μA/cm^2, and the E_{corr} was −0.049 mV. The I_{corr} values of the electrodes coated with coatings significantly increased in the range from 3.456×10^{-3} to 3.864×10^{-6} μA/cm^2, and the values of E_{corr}, correspondingly, increased from 0.125 to 0.201 mV. It was clear that all coatings manifested high protection efficiencies compared to the bare steel. However, a higher content of PEG in the polybenzoxazine coating facilitated the corrosive medium contacting with the metal surface, and the coating displayed a larger I_{corr} and lower PE value. A reasonable explanation was given that the hydrophilicity of PEG in the coating tended to maximize the absorption of water, and accelerated the diffusion of the water in the coating. The water contact angles of the different coatings are shown in Table S4. The contact angle of PCB coating was 107.88°, while the values of PCBG coatings were regularly decreased in the range from 103.04 to 78.32°. These indicated that the water adsorption capacity of the coating could be increased when a higher content of PEG was blended in the coating.

The corrosion resistance of steel and different coatings (23 ± 3 μm) was evaluated in the 3.5 wt% NaCl solution. The impedance modulus at lower frequency (|Z| = 0.01 Hz) is a vital parameter which measures the barrier effect of a coating [66]. As shown in Fig. 9 (a) and Fig. S8 (a), the impedance modulus of the coatings increased by approximately 3–7 orders than that of the bare steel after 0.5 h immersion. With immersion time, the impedance modulus of all coatings decreased to some degrees. The PCBG-20 and PCBG-30 decreased significantly due to the rapid water adsorption. Obviously, the PCB, PCBG-10 and PCBG-15 continuously displayed a conspicuous barrier effect in 2616 h, 672 h, and 504 h

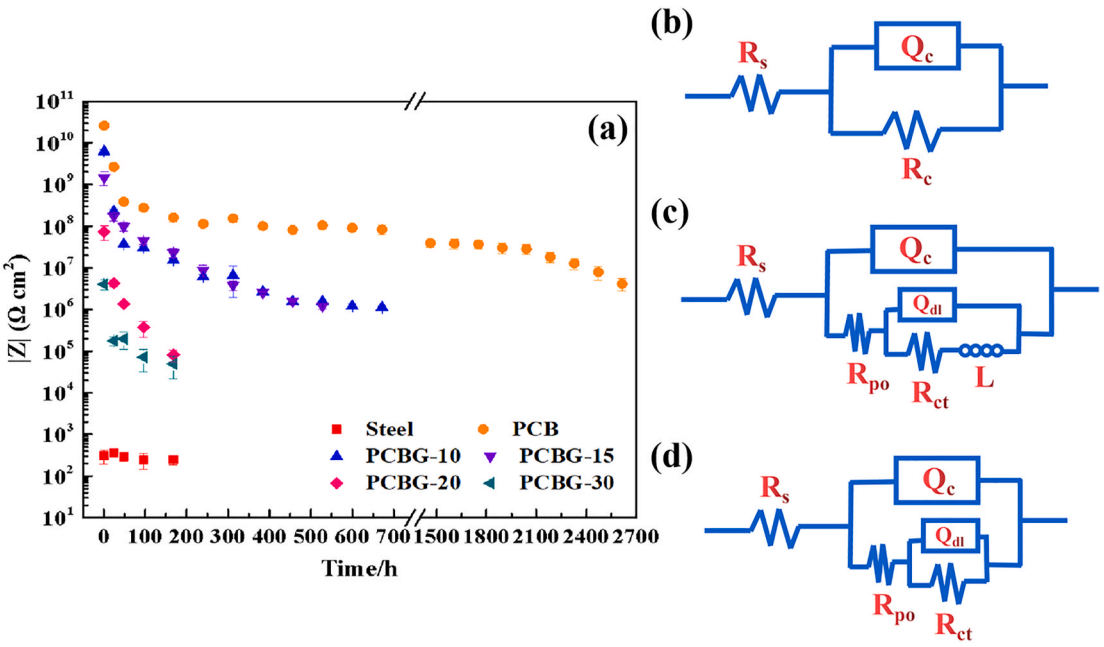

Fig. 9. (a) EIS Module results of different coatings at lower frequency (|Z| = 0.01 Hz), and equivalent circuits used for EIS analysis of different coatings in the (b, c) initial, (d) middle and later stages.

of immersion, respectively. From 456 h to 2328 h, the impedance module of the PCB coating steadily reduced in the range from 8.163 × 10^7 Ω cm^2 to 1.280 × 10^7 Ω cm^2. Then, the value of PCB coating rapidly decreased after 2616 h immersion, indicating that the coating was seriously damaged after water penetration.

To monitor the coating protectiveness varying with immersion time, the EIS spectra of the coatings were measured, and the Nyquist plots and the Bode plots are presented in Fig. 10 and Fig. S8 (a-b). The decreased modules of different coatings in Fig. S8 (a) obviously indicated the declining anticorrosion capacity of coatings as a barrier with time. As shown in Fig. S8 (b), the presence of two time-constants implied that corrosion was occurring on the substrate because the corrosive medium had arrived at the substrate [67]. The PCBG-20 and PCBG-30 coatings had two time-constants after 48 h immersion, indicating that the corrosive medium arrived at the metal substrate, while PCB, PCBG-10 and PCBG-15 coatings always showed only one time-constant, which suggested that the corrosive medium had not penetrated though the coating and the coating was a very effective barrier. The impedance data are fitted using the equivalent circuits (Fig. 9 b through d). The fitted electrochemical parameters include the solution resistance (R_s), coating resistance (R_c), coating pore resistance (R_{po}), charge transfer resistance (R_{ct}), constant phase element of coating (Q_c), constant phase element of double layer (Q_{dl}), and induce reactance (L). The EIS spectra in the initial immersion period is simulated by the R(QR) circuit for PCB coating and the R(Q(R(Q(RL)))) circuit for PCBG coatings. The EIS spectra of coatings in the middle and later immersion periods are simulated by the R(Q(R(QR))) circuit, as shown in Fig. 9(b–d). The Nyquist plots of the steel and different coatings were continuously measured over a long period of time (see in Fig. 10), and the detailed fitting values of electrochemical parameters in the initial, middle and later immersing periods are shown in Tables 2–4, respectively. All the coatings had an increasing water adsorption behavior, indicating that the corrosive ions had permeated and slowly diffused in the coatings, as shown in Fig. S9. Compared with the other composite PCBG coatings, the PCB showed good water adsorption resistance, implying that this coating had great protection performance. The PCBG-20 and PCBG-30 coatings exhibited intensive water adsorption that caused rapid penetration of corrosive medium through the coatings after 144 h and 168 h respectively to attack the substrate metal. The capacitive loops of the PCBG-10 and PCBG-15 coatings significantly decreased in 672 h and 504 h, respectively. The coatings were subjected to the infiltration of corrosive medium, and the attack of the corrosive medium to coating surface generated pores and cracks in the coating, eventually damaging the coating. The PCB developed the highest overall capacitive arcs among all the coatings studied herein even after 2616 h immersion (see Fig. 10). The typical anticorrosion capacity of the PCB coating favored the creation of an outstanding effective barrier to prevent the metal from corrosion in a long-term. This was supported by the electrochemical parameters listed in Tables 2–4. For example, the R_c value in the initial period and the R_{po} value of the PCB coating in the middle and latter periods decreased from 3.445 × 10^{10} to 5.322 × 10^6 and then 1.264 × 10^6 Ω cm^2 after 0.5, 1320 and 2616 h immersion. Besides, the R_{po} value of the PCBG-10 coating reduced from 1.291 × 10^6 to 9.609 × 10^5 and 9.613 × 10^5 Ω cm^2 after 0.5, 312 and 672 h immersion. Meanwhile, the R_{po} value of the PCBG-15 coating decreased from 5.002 × 10^6 to 1.902 × 10^6 and 1.056 × 10^6 Ω cm^2 after 0.5, 264, and 504 h immersion. The above results showed that the R_{po} value of the PCB coating was higher than those of the PCBG-10 and PCBG-15 coatings, although the immersion time of the PCB was longer than those of the other coatings in the middle and later periods. Meanwhile, the Q_c values of the PCBG-10 and PCBG-15 coatings increased from 2.154 × 10^{-10} to 3.268 × 10^{-9} $Ω^{-1}cm^{-2}s^n$, and from 2.081 × 10^{-10} to 3.263 × 10^{-9} $Ω^{-1}cm^{-2}s^n$ after 672 h and 504 h immersion, respectively. While the Q_c value of the PCB coating had no obviously change even after 2616 h immersion. An increase in Q_c corresponds to a water adsorption behavior in an organic coating. Thus, the PCB coating had better resistance of water adsorption than that of the PCBG-10 and PCBG-15 coatings, and the PCB coating could protect the metal substrate from contacting the corrosive medium to avoid the corrosion reaction.

In order to obtain a deep insight into the corrosion resistant behaviors of the bare steel and different coatings, their optical microscopic and SEM images before and after the salt immersion are presented in Fig. 11. The bright surface of bare steel turned into a large amount of green rust after 7 day immersion. Meanwhile, the PCBG-20 and PCBG-30 coatings had lots of bubbles on their surfaces after 7 and 2 days of immersion, and pores appeared on the coating surfaces (see Fig. 11 (C)). Besides, the PCBG-10 and PCBG-15 coatings became ineffective after 28 and 21 days of immersion due to the presence of pores. Meanwhile, the optical

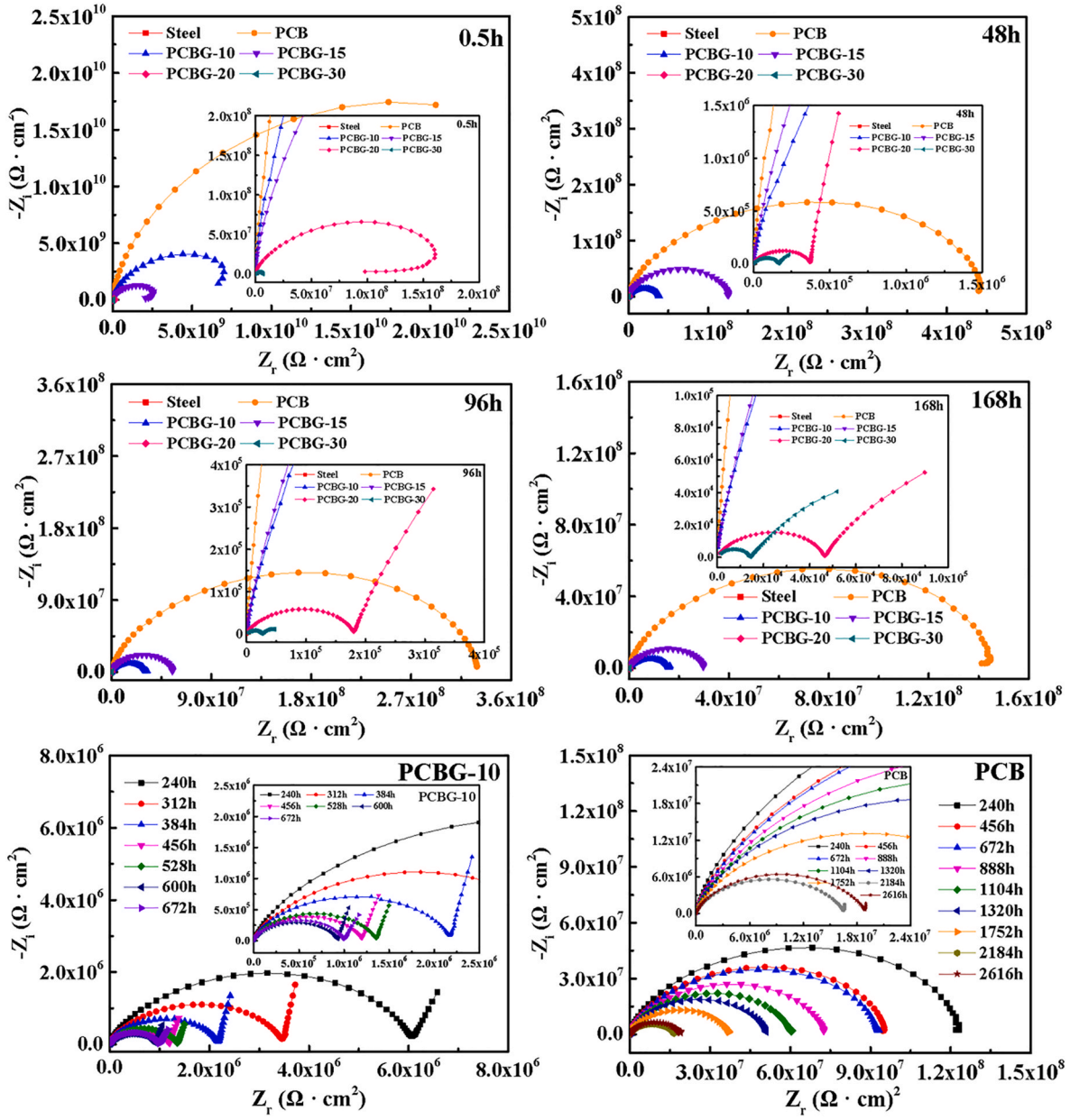

Fig. 10. EIS Nyquist spectra of different coatings after immersion in 3.5 wt% NaCl solution for different periods of time.

Table 2
Electrochemical parameters fitted from the equivalent circuits in the initial period.

	R_s/Ω·cm^2	Q_c (Ω^{-1}cm^{-2}s^n)	n_1	R_c/Ω·cm^2	R_{po}/Ω·cm^2	Q_{dl} (Ω^{-1}cm^{-2}s^n)	n_2	R_{ct} /Ω·cm^2	L_w//Ω·cm^2
PCB-0.5h	1×10^3	2.444×10^{-10}	0.969	3.445×10^{10}					
PCBG-10-0.5h	1×10^3	2.154×10^{-10}	0.983		1.291×10^6	1.848×10^{-10}	0.3065	1.747×10^{10}	1.067×10^{11}
PCBG-15-0.5h	1×10^3	2.081×10^{-10}	0.980		5.002×10^6	4.328×10^{-10}	0.2722	4.628×10^9	2.041×10^{10}

Table 3
Electrochemical parameters fitted from the equivalent circuit in the middle period.

	R_s/Ω·cm^2	Q_c (Ω^{-1}cm^{-2}s^n)	n_1	R_{po}/Ω·cm^2	Q_{dl} (Ω^{-1}cm^{-2}s^n)	n_2	R_{ct} /Ω·cm^2
PCB-1320h	1×10^3	4.068×10^{-10}	0.9530	5.322×10^6	1.436×10^{-9}	0.6952	4.662×10^7
PCBG-10-312h	1×10^3	3.268×10^{-9}	0.8188	9.609×10^5	1.459×10^{-5}	0.6687	2.190×10^7
PCBG-15-264h	1×10^3	7.270×10^{-10}	0.9138	1.902×10^6	3.856×10^{-9}	0.6908	1.005×10^7

Table 4
Electrochemical parameters fitted from the equivalent circuit in the later period.

	$R_s/\Omega\cdot cm^2$	Q_c ($\Omega^{-1}cm^{-2}s^n$)	n_1	$R_{po}/\Omega\cdot cm^2$	Q_{dl} ($\Omega^{-1}cm^{-2}s^n$)	n_2	R_{ct} $/\Omega\cdot cm^2$
PCB-2616h	1×10^3	4.284×10^{-10}	0.9607	1.264×10^6	3.042×10^{-9}	0.6336	1.807×10^7
PCBG-10-672h	1×10^3	3.271×10^{-9}	0.8187	9.613×10^5	1.474×10^{-5}	0.6748	1.311×10^7
PCBG-15-504h	1×10^3	3.263×10^{-9}	0.8046	1.056×10^6	1.239×10^{-5}	0.7891	1.000×10^7

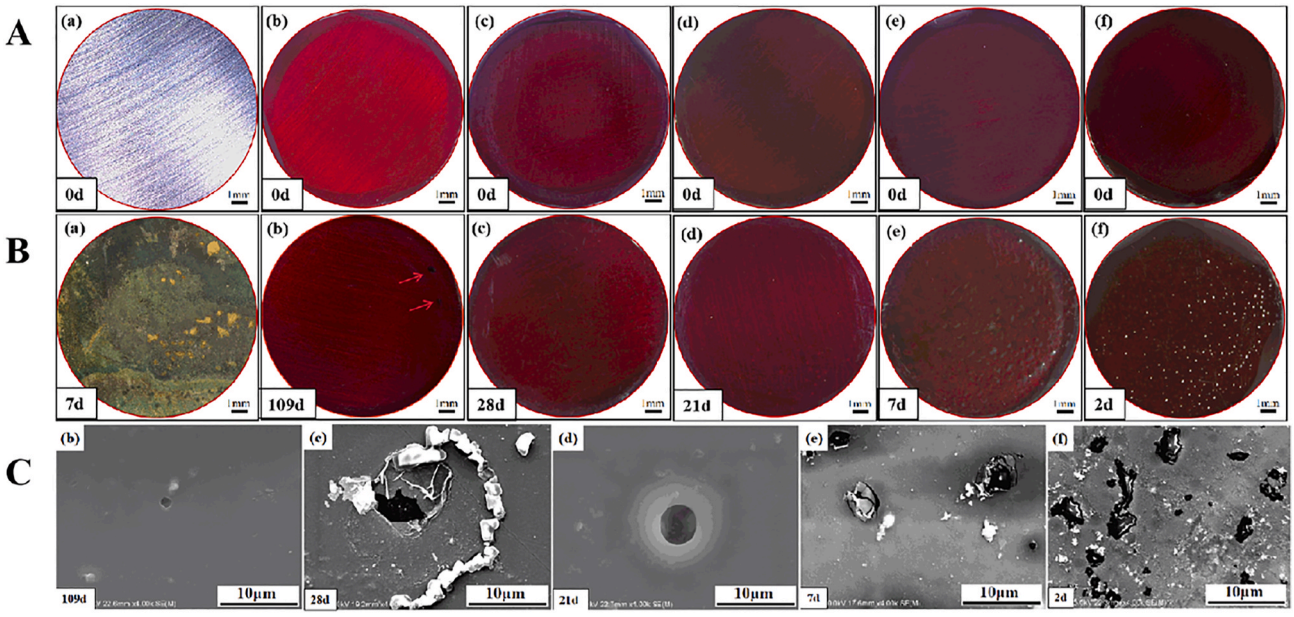

Fig. 11. The (A and B) Leica microscopic and (C) SEM images of different coatings before and after immersion in 3.5 wt% NaCl solution: (a) bare steel, (b) PCB coating, (c) PCBG-10 coating, (d) PCBG-15 coating, (e) PCBG-20 coating, and (f) PCBG-30 coating.

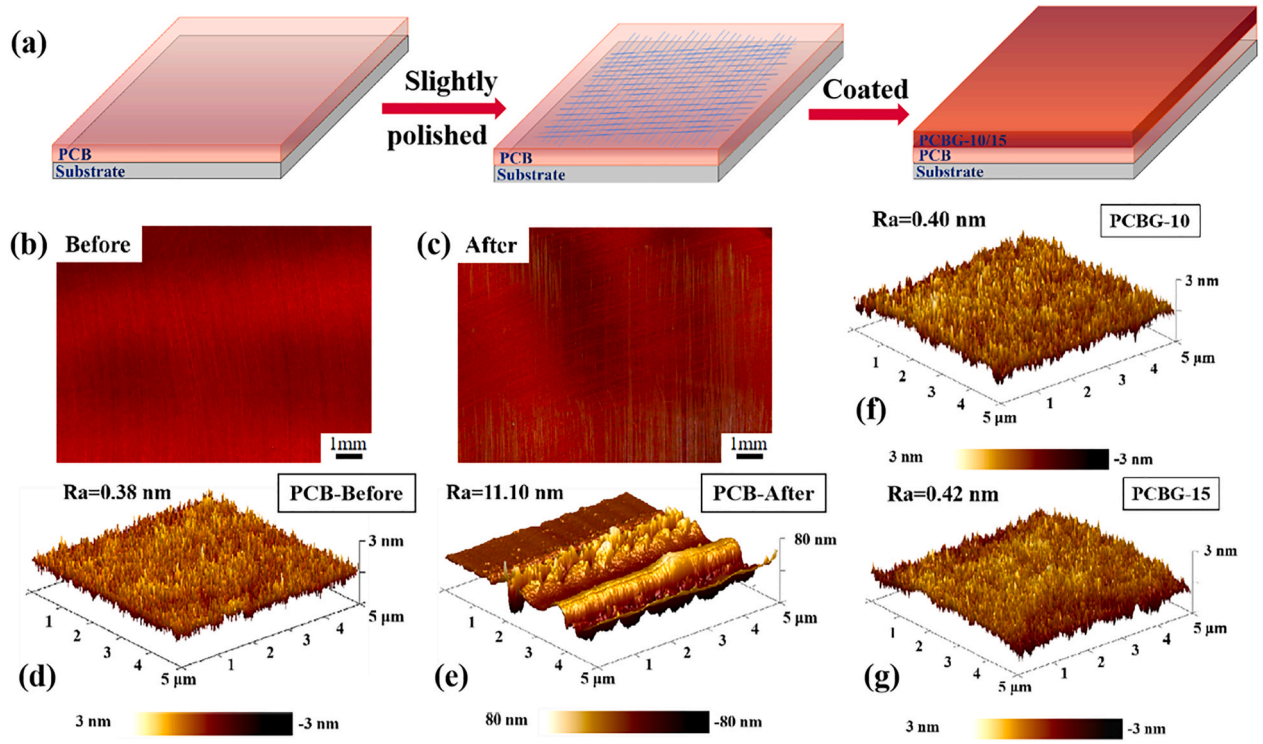

Fig. 12. (a) Schematic illustration of a coating system design, microscopic images of coating PCB (b) before and (c) after slightly polishing, AFM roughness images of coating PCB (d) before and (e) after polishing, and AFM roughness images of coatings (f) P10 and (g) P15.

microscopic images of the PCB coating were recorded at different immersion periods as shown in Fig. S10. It was observed that the PCB coating maintained a bright surface and excellent integrity even after longer immersion for 92 days. However, the coating was found to have micro-pores which could reduce the protectiveness after a longer exposure for 109 days in the corrosive medium. Thus, rust was found at the PCB coating/substrate interface, as shown in Fig. 11 (B). Therefore, the electrochemical results revealed that the PCB possessed the superior corrosion-resistance to prevent the metal substrate in the 3.5 wt% NaCl solution, indicating that the good shielding effect of the coating came from the inherent properties of the polybenzoxazine resin, including low water absorption and a high cross-linking density reinforced by the cooperative interaction between Si–O–Si linkages and Mannich bridge portion, as shown in Fig. 6 (a).

In the above antifouling and anticorrosion tests, the coatings were measured to have a stable anti-corrosion behavior and anti-microalgae fouling property in the 3.5 wt% NaCl solution and the artificial sea water. They are expected to be stable in other corrosive environments as well.

2.4. A design of coating system for anticorrosion and antifouling activities

The above coatings could not have good anti-fouling and anti-corrosion properties in the same time. Specifically, the coatings PCBG-10 and PCBG-15 exhibited a great antifouling capability, but their corrosion resistance was low. To possess high corrosion resistance and anti-fouling performance simultaneously, a double-layer coating system was designed with the PCB as the sub-layer and the PCBG-10 or PCBG-15 as the up-layer. In this model as shown in Fig. 12 (a), the PCB was directly coated on the substrate as the priming paint that had a dry thickness of 20 ± 3 μm. It acted as the layer to prevent the substrate from the corrosive medium attack. The as-prepared surface of the sub-layer was slightly polished for a firm contact with the up-layer PCBG-10 or PCBG-15 with a dry thickness of 10 ± 3 μm. These up-layers could achieve a highly efficient antifouling. The designed coating system is named as P10 or P15. The microscopic images of the PCB were shown in Fig. 12 (b and c) before and after polishing. The minimum roughness R_a value of the PCB before polishing was 0.38 nm in an area of 5 μm × 5 μm measured by AFM microscopy, and the value gradually increased to 11.10 nm after polishing. When 30 ± 5 μm of the PCBG-10 and PCBG-15 coated on the polished surface, their roughness values were measured to be 0.40 nm and 0.42 nm, respectively, as shown in Fig. 12 (f and g), indicating that the surfaces were very smooth.

A series of measurements were conducted to investigate the corrosion performance of the coatings by means of EIS on the designed model coatings P10 and P15 under the salt immersion at 23 °C and the salt-spray at 35 °C. The EIS Nyquist results, Bode plots of the P10 and P15 are showed in Fig. 13, Fig. S11 (a-d) and Fig. S12 (a-d). The capacitive arcs of the P10 and P15 gradually decreased after the long-time exposure in the corrosive media (see Fig. 13). As shown in Fig. S11, the impendence modulus at low frequency 10^{-2} Hz ($|Z|_{0.01\ Hz}$) well reflected the corrosion-resistance of the coatings in the different corrosion media. The $|Z|_{0.01\ Hz}$ values of the P10 and P15 coating in immersion were 6.53 × 10^{10} Ω cm^2 and 4.57 × 10^{10} Ω cm^2, while they sharply decreased by about 3 orders of magnitude to 6.01 × 10^7 Ω cm^2 and 2.32 × 10^7 Ω cm^2 after 180 days of immersion in the 3.5 wt% NaCl solution (see Fig. S11 (a and b)). Besides, in the salt spray, the $|Z|_{0.01\ Hz}$ values of the P10 and P15 were higher around 3.22 × 10^8 Ω cm^2 and 4.06 × 10^9 Ω cm^2, respectively, but they sharply dropped by about 1–2 orders of magnitude down to 3.69 × 10^7 Ω cm^2 and 6.87 × 10^7 Ω cm^2 after 150 day exposure in the salt-spray (see Fig. S11 (c and d)). The corrosive medium should have penetrated through the micro-pores and/or defects in the coating, reducing the barrier effect of the coatings. The above results suggested that the designed model coatings P10 or P15 had great anti-corrosion performance due to their long-term barrier effect in the different corrosive media. Obviously, in the Bode-phase plots (see Fig. S12 (a-d)), the P10 and P15 always exhibited one time constant in the 180 days of immersion or the 150 days of salt spray, as shown in Fig. S12 (a-d).

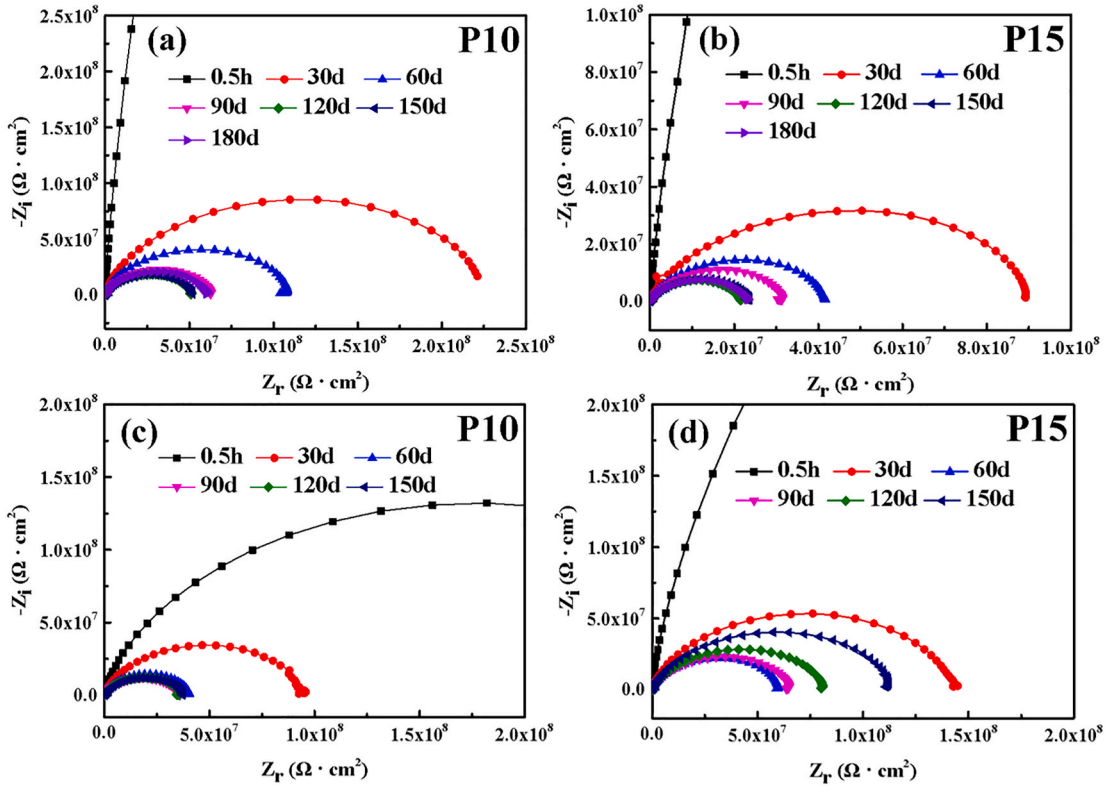

Fig. 13. EIS Nyquist spectra of coatings P10 and P15 after (a, b) immersion in 3.5 wt% NaCl solution and (c, d) exposure in 5.0 wt% NaCl salt-spray.

These indicated that the corrosive medium had not penetrated through the coatings and reached the metal substrate after the long-term exposure, and the coatings acted as an effective barrier layer, having great anticorrosion performance.

Different from many reported coatings that have some specific functional properties because of the addition of modified inorganic fillers [66,68–73], the curcumin-based polybenzoxazine coating in this study possesses the corrosion resistance and antifouling performance due to the specifically designed structure of the coating framework. This unique structure ensures the following advantages of the coating over others: Firstly, the polybenzoxazine coating performs the excellently low water adsorption to retard the water penetration. Secondly, the Si–O–Si groups in the coating not only increase the framework crosslinking to enhance the anticorrosion, but also decrease the coating surface free energy to reduce the attachment of fouling species. Thirdly, the curcumin implanted in the polybenzoxazine skeleton can promote the antifouling performance of the coating due to its inherent antibacterial characteristic. Finally, the existence of the PEG chains in the coating can adjust the physical and mechanical properties, and strikingly improve the antifouling capacity. To develop excellent comprehensive performance, the PCB coating was used as the sub-layer to prevent the substrate from corrosion, and the PCBG-10 coating (10 wt% content of PEG in the coating) was used as the up-layer to retard the attachment of fouling species.

3. Conclusions

In this paper, to meet the sustainable, low-cost and highly effective requirements, a series of new multi-functional double-layer coatings were developed, which could prevent not only the settlement, adhesion, and growth of microorganisms, but also corrosion attack. These high-performance polybenzoxazine coatings were synthesized using curcumin, 3-aminopropyltriethoxysilane and paraformaldehyde, and the curcumin-based polybenzoxazine could be used as a sub-layer protecting barrier that effectively prevented the substrate metal from corrosion attack in corrosive environments. The coating showed impressive long-term corrosion resistance even after exposure in different corrosive environments for months. Via cooperative interaction between curcumin and PEG chain in the polybenzoxazine resin framework, this coating could also be used as an up-layer, because it had a strong hydration layer and high interaction energy at molecule level and thus an outstanding anti-fouling ability against the adsorption of protein or the attachment of bacteria and microalgae. It is expected that this double layer coating system can enable various applications in the marine industry, as well as relevant fields.

Credit author statement

Yajun Deng: Investigation; Methodology, Data curation, Writing -original draft, **Lixue Xia:** Investigation; Methodology, Data curation, **Guang-Ling Song**: Funding acquisition, Project administration, Supervision, Conceptualization, Formal analysis, Investigation; Methodology, Writing –review & editing, **Yan Zhao:** Funding acquisition, Project administration, Supervision, Formal analysis, Investigation; Methodology, **Yanmei Zhang:** Methodology, Data curation, **Yuqing Xu:** Methodology, Data curation, **Da-Jiang Zheng**: Methodology, Resources, Software.

Author contributions

Y. Deng and L. Xia contributed equally to this work.

Declaration of competing interest

The authors declare that they have no known competing financial interests or personal relationships that could have appeared to influence the work reported in this paper.

Acknowledgements

The support of the National Key Research and Development Program of China (Grant No. 2017YFB0702100) and the National Natural Science Foundation of China (key project Grant No.51731008, general project Grant No.51671163 and No.51901198) is acknowledged. This work also supported by Foshan Xianhu Laboratory of the Advanced Energy Science and Technology Guangdong Laboratory (XHT2020-003) and Fundamental Research Funds for the Central Universities (WUT:2020III029, 2020IVA100).

Appendix A. Supplementary data

Supplementary data to this article can be found online at https://doi.org/10.1016/j.compositesb.2021.109263.

References

[1] Kotzebue LRV, de Oliveira JR, da Silva JB, Mazzetto SE, Ishida H, Lomonaco D. Development of fully biobased high-performance bis-benzoxazine under environmentally friendly conditions. ACS Sustainable Chem Eng 2018;6(4):5485–94.
[2] Shi W, Zhang X, Ji Y, Zhao Z, Li W, Jia X. Sustainable preparation of bio-based polybenzoxazine resins from amino acid and their application in CO_2 adsorption. ACS Sustainable Chem Eng 2019;7(20):17313–24.
[3] Oliveira JR, Kotzebue LRV, Freitas DB, Mattos ALA, da Costa Júnior AE, Mazzetto SE, et al. Towards novel high-performance bio-composites: polybenzoxazine-based matrix reinforced with Manicaria saccifera fabrics. Compos B Eng 2020;194:108060.
[4] Peng C, Wu Z, Zhou D. Synthesis of a benzoxazine-type dispersant and its application on epoxy/benzoxazine/ZrO_2 composite: dispersion performance and tensile behavior. Compos B Eng 2019;167:507–16.
[5] Moore CJ. Synthetic polymers in the marine environment: a rapidly increasing, long-term threat. Environ Res 2008;108(2):131–9.
[6] Zhang K, Han M, Liu Y, Froimowicz P. Design and synthesis of bio-based high-performance trioxazine benzoxazine resin via natural renewable resources. ACS Sustainable Chem Eng 2019;7(10):9399–407.
[7] Anastas PT, Warner J. Green chemistry: theory and practice. 1998.
[8] Wang H, Wang J, He X, Feng T, Ramdani N, Luan M, et al. Synthesis of novel furan-containing tetrafunctional fluorene-based benzoxazine monomer and its high performance thermoset. RSC Adv 2014;4(110):64798–801.
[9] Dumas L, Bonnaud L, Olivier M, Poorteman M, Dubois P. Eugenol-based benzoxazine: from straight synthesis to taming of the network properties. J Mater Chem A 2015;3(11):6012–8.
[10] Thirukumaran P, Shakila A, Muthusamy S. Synthesis and characterization of novel bio-based benzoxazines from eugenol. RSC Adv 2014;4(16):7959–66.
[11] Thirukumaran P, Shakila Parveen A, Sarojadevi M. Synthesis and copolymerization of fully biobased benzoxazines from renewable resources. ACS Sustainable Chem Eng 2014;2(12):2790–801.
[12] Dumas L, Bonnaud L, Olivier M, Poorteman M, Dubois P. Chavicol benzoxazine: ultrahigh Tg biobased thermoset with tunable extended network. Eur Polym J 2016;81:337–46.
[13] Lyu Y, Ishida H. Natural-sourced benzoxazine resins, homopolymers, blends and composites: a review of their synthesis, manufacturing and applications. Prog Polym Sci 2019;99:101168–224.
[14] Sini NK, Bijwe J, Varma IK. Renewable benzoxazine monomer from Vanillin: synthesis, characterization, and studies on curing behavior. J Polym Sci Part A Polym Chem 2014;52(1):7–11.
[15] Van A, Chiou K, Ishida H. Use of renewable resource vanillin for the preparation of benzoxazine resin and reactive monomeric surfactant containing oxazine ring. Polym 2014;55(6):1443–51.
[16] Xu H, Lu Z, Zhang G. Synthesis and properties of thermosetting resin based on urushiol. RSC Adv 2012;2(7):2768–72.
[17] Thirukumaran P, Sathiyamoorthi R, Shakila Parveen A, Sarojadevi M. New benzoxazines from renewable resources for green composite applications. Polym Compos 2016;37(2):573–82.
[18] Chen Y-P, He X-Y, Dayo AQ, Wang J-Y, Liu W-b, Wang J, et al. Synthesis and characterization of cardanol containing tetra-functional fluorene-based benzoxazine resin having two different oxazine ring structures. Polym 2019;179:121620.
[19] Wang C, Sun J, Liu X, Sudo A, Endo T. Synthesis and copolymerization of fully bio-based benzoxazines from guaiacol, furfurylamine and stearylamine. Green Chem 2012;14(10):2799–806.
[20] Comí M, Lligadas G, Ronda JC, Galià M, Cádiz V. Renewable benzoxazine monomers from "lignin-like" naturally occurring phenolic derivatives. J Polym Sci Part A Polym Chem 2013;51(22):4894–903.

[21] Kiskan B, Yagci Y. Thermally curable benzoxazine monomer with a photodimerizable coumarin group. J Polym Sci Part A Polym Chem 2007;45(9):1670–6.
[22] Froimowicz P RArza C, Han L, Ishida H. Smart, sustainable, and ecofriendly chemical design of fully bio-based thermally stable thermosets based on benzoxazine chemistry. ChemSusChem 2016;9(15):1921–8.
[23] Heo DN, Ko W-K, Moon H-J, Kim H-J, Lee SJ, Lee JB, et al. Inhibition of osteoclast differentiation by gold nanoparticles functionalized with cyclodextrin curcumin complexes. ACS Nano 2014;8(12):12049–62.
[24] Barry J, Fritz M, Brender JR, Smith PES, Lee D-K, Ramamoorthy A. Determining the effects of lipophilic drugs on membrane structure by solid-state NMR spectroscopy: the case of the antioxidant curcumin. J Am Chem Soc 2009;131(12):4490–8.
[25] Das RK, Kasoju N, Bora U. Encapsulation of curcumin in alginate-chitosan-pluronic composite nanoparticles for delivery to cancer cells. Nanomed Nanotechnol Biol Med 2010;6(1):153–60.
[26] Xie J, Yong Y, Dong X, Du J, Guo Z, Gong L, et al. Therapeutic nanoparticles based on curcumin and bamboo charcoal nanoparticles for chemo-photothermal synergistic treatment of cancer and radioprotection of normal cells. ACS Appl Mater Interfaces 2017;9(16):14281–91.
[27] Patil DM, Phalak GA, Mhaske ST. Synthesis and characterization of bio-based benzoxazine oligomer from cardanol for corrosion resistance application. J Coating Technol Res 2017;14(3):517–30.
[28] Ngo BKD, Grunlan MA. Protein resistant polymeric biomaterials. ACS Macro Lett 2017;6(9):992–1000.
[29] Gillich T, Benetti EM, Rakhmatullina E, Konradi R, Li W, Zhang A, et al. Self-assembly of focal point oligo-catechol ethylene glycol dendrons on titanium oxide surfaces: adsorption kinetics, surface characterization, and nonfouling properties. J Am Chem Soc 2011;133(28):10940–50.
[30] Zhou W, Rao Y, Zhuang W, Ge L, Lin R, Tang T, et al. Improved enzymatic activity by oriented immobilization on graphene oxide with tunable surface heterogeneity. Compos B Eng 2021;216:108788.
[31] Xing C-M, Meng F-N, Quan M, Ding K, Dang Y, Gong Y-K. Quantitative fabrication, performance optimization and comparison of PEG and zwitterionic polymer antifouling coatings. Acta Biomater 2017;59:129–38.
[32] Goh SC, Luan Y, Wang X, Du H, Chau C, Schellhorn HE, et al. Polydopamine–polyethylene glycol–albumin antifouling coatings on multiple substrates. J Mater Chem B 2018;6(6):940–9.
[33] Yandi W, Mieszkin S, Martin-Tanchereau P, Callow ME, Callow JA, Tyson L, et al. Hydration and chain entanglement determines the optimum thickness of poly (HEMA-co-PEG10MA) brushes for effective resistance to settlement and adhesion of marine fouling organisms. ACS Appl Mater Interfaces 2014;6(14):11448–58.
[34] Phalak GA, Patil DM, Mhaske ST. Synthesis and characterization of thermally curable guaiacol based poly(benzoxazine-urethane) coating for corrosion protection on mild steel. Eur Polym J 2017;88:93–108.
[35] Aydogan C, Kiskan B, Hacioglu SO, Toppare L, Yagci Y. Electrochemical manipulation of adhesion strength of polybenzoxazines on metal surfaces: from strong adhesion to dismantling. RSC Adv 2014;4(52):27545–51.
[36] Kudoh R, Sudo A, Endo T. A highly reactive benzoxazine monomer, 1-(2-hydroxyethyl)-1,3-benzoxazine: activation of benzoxazine by neighboring group participation of hydroxyl group. Macromolecules 2010;43(3):1185–7.
[37] Zhu Y, Su J, Lin R, Li P. Improving the thermal stability of polybenzoxazines through incorporation of eugenol-based benzoxazine. Macromol Res 2020;28(5):472–9.
[38] Ren S, Miao X, Zhao W, Zhang S, Wang W. A fully bio-based benzoxazine as latent catalyst for bisphenol A/aniline-based benzoxazine. Mater Today Commun 2019;20:100568.
[39] Liu J, Lu X, Xin Z, Zhou C. Synthesis and surface properties of low surface free energy silane-functional polybenzoxazine films. Langmuir 2013;29(1):411–6.
[40] Agag T, Takeichi T. Synthesis and characterization of benzoxazine resin-SiO_2 hybrids by sol-gel process: the role of benzoxazine-functional silane coupling agent. Polym 2011;52(13):2757–63.
[41] Zhao S, Pei L, He J, Zhang X, Hu W, Yan H, et al. Curing mechanism, thermal and ablative properties of hexa-(4-amino-phenoxy) cyclotriphosphazene/benzoxazine blends. Compos B Eng 2021;216:108838.
[42] Arslan M, Kiskan B, Yagci Y. Benzoxazine-based thermosets with autonomous self-healing ability. Macromolecules 2015;48(5):1329–34.
[43] Cavallaro G, Lazzara G, Massaro M, Milioto S, Noto R, Parisi F, et al. Biocompatible poly(N-isopropylacrylamide)-halloysite nanotubes for thermoresponsive curcumin release. J Phys Chem C 2015;119(16):8944–51.
[44] Deng Y, Song G-L, Zheng D, Zhang Y. Fabrication and synergistic antibacterial and antifouling effect of an organic/inorganic hybrid coating embedded with nanocomposite Ag@TA-SiO_2 particles. Colloids Surf A Physicochem Eng Asp 2021;613:126085.
[45] Ran J, Qiu J, Xie H, Lai X, Li H, Zeng X. Combination effect of zirconium phosphate nanosheet and PU-coated carbon fiber on flame retardancy and thermal behavior of PA46/PPO alloy. Compos B Eng 2019;166:621–32.
[46] Fang B, Lu X, Hu J, Zhang G, Zheng X, He L, et al. pH controlled green luminescent carbon dots derived from benzoxazine monomers for the fluorescence turn-on and turn-off detection. J Colloid Interface Sci 2019;536:516–25.
[47] Lu Y-C, Chen J, Wang A-J, Bao N, Feng J-J, Wang W, et al. Facile synthesis of oxygen and sulfur co-doped graphitic carbon nitride fluorescent quantum dots and their application for mercury(ii) detection and bioimaging. J Mater Chem C 2015;3(1):73–8.
[48] Wu J-Y, Mohamed MG, Kuo S-W. Directly synthesized nitrogen-doped microporous carbons from polybenzoxazine resins for carbon dioxide capture. Polym Chem 2017;8(36):5481–9.
[49] Leane MM, Nankervis R, Smith A, Illum L. Use of the ninhydrin assay to measure the release of chitosan from oral solid dosage forms. Int J Pharm 2004;271(1):241–9.
[50] Sharma P, Dutta P, Nebhani L. Sustainable approach towards enhancing thermal stability of bio-based polybenzoxazines. Polym 2019;184:121905.
[51] Drumond WS, Mothé CG, Wang SH. Quantitativeanalysis of biodegradable amphiphilic poly(L-lactide)-block-poly(ethyleneglycol)-blockpoly(L-lactide) by using TG, FTIR and NMR. J Therm Anal Calorim 2006;85(1):173–7.
[52] Zhang Z, Fan GD, Yang HY. Study on chain extension and modification of poly (lactic acid) by isophorone diisocyanate/polyethylene glycol. Adv Mater Res 2012;476–478:2067–70.
[53] Dexter SC. Influence of substratum critical surface tension on bacterial adhesion—in situ studies. J Colloid Interface Sci 1979;70(2):346–54.
[54] Baier RE, Meyer AE. Surface analysis of fouling-resistant marine coatings. Biofouling 1992;6(2):165–80.
[55] Zhao Q. Effect of surface free energy of graded NI–P–PTFE coatings on bacterial adhesion. Surf Coating Technol 2004;185(2):199–204.
[56] Harder P, Grunze M, Dahint R, Whitesides GM, Laibinis PE. Molecular conformation in oligo(ethylene glycol)-terminated self-assembled monolayers on gold and silver surfaces determines their ability to resist protein adsorption. J Phys Chem B 1998;102(2):426–36.
[57] Zhao Y-Q, Sun Y, Zhang Y, Ding X, Zhao N, Yu B, et al. Well-defined gold nanorod/polymer hybrid coating with inherent antifouling and photothermal bactericidal properties for Treating an infected hernia. ACS Nano 2020;14(2):2265–75.
[58] Sheikh S, Blaszykowski C, Nolan R, Thompson D, Thompson M. On the hydration of subnanometric antifouling organosilane adlayers: a molecular dynamics simulation. J Colloid Interface Sci 2015;437:197–204.
[59] Prime KL, Whitesides GM. Adsorption of proteins onto surfaces containing end-attached oligo(ethylene oxide): a model system using self-assembled monolayers. J Am Chem Soc 1993;115(23):10714–21.
[60] Chen Q, Yu S, Zhang D, Zhang W, Zhang H, Zou J, et al. Impact of antifouling PEG layer on the performance of functional peptides in regulating cell behaviors. J Am Chem Soc 2019;141(42):16772–80.
[61] Szleifer I. Polymers and proteins: interactions at interfaces. Curr Opin Solid State Mater 1997;2(3):337–44.
[62] Szleifer I. Protein adsorption on tethered polymer layers: effect of polymer chain architecture and composition. Physica A 1997;244(1):370–88.
[63] Hu J, Lin J, Zhang Y, Lin Z, Qiao Z, Liu Z, et al. A new anti-biofilm strategy of enabling arbitrary surfaces of materials and devices with robust bacterial anti-adhesion via a spraying modified microsphere method. J Mater Chem A 2019;7(45):26039–52.
[64] Natarajan KA. Chapter 12 - biofouling and microbially influenced corrosion. In: Natarajan KA, editor. Biotechnology of metals. Amsterdam: Elsevier; 2018. p355–93.
[65] Li Y, Ning C. Latest research progress of marine microbiological corrosion and biofouling, and new approaches of marine anti-corrosion and anti-fouling. Bioact Mater 2019;4:189–95.
[66] Yan D, Liu J, Zhang Z, Wang Y, Zhang M, Song D, et al. Dual-functional graphene oxide-based nanomaterial for enhancing the passive and active corrosion protection of epoxy coating. Compos B Eng 2021;222:109075.
[67] Cheng L, Wu H, Li J, Zhao H, Wang L. Polydopamine modified ultrathin hydroxyapatite nanosheets for anti-corrosion reinforcement in polymeric coatings. Corrosion Sci 2021;178:109064.
[68] Cui J, Xu J, Li J, Qiu H, Zheng S, Yang J. A crosslinkable graphene oxide in waterborne polyurethane anticorrosive coatings: experiments and simulation. Compos B Eng 2020;188:107889.
[69] Ai Y-F, Xia L, Pang F-Q, Xu Y-L, Zhao H-B, Jian R-K. Mechanically strong and flame-retardant epoxy resins with anti-corrosion performance. Compos B Eng 2020;193:108019.
[70] Haddadi SA, Mehmandar E, Jabari H, Ramazani SAA, Mohammadkhani R, Yan N, et al. Zinc-doped silica/polyaniline core/shell nanoparticles towards corrosion protection epoxy nanocomposite coatings. Compos B Eng 2021;212:108713.
[71] Cheng M, Li F, Wang Z, Li C, Sun S, Hu S. New valve-free organosilica nanocontainer for active anticorrosion of polymer coatings. Compos B Eng 2021;224:109185.
[72] Muthulakshmi L, Varada Rajalu A, Kaliaraj GS, Siengchin S, Parameswaranpillai J, Saraswathi R. Preparation of cellulose/copper nanoparticles bionanocomposite films using a bioflocculant polymer as reducing agent for antibacterial and anticorrosion applications. Compos B Eng 2019;175:107177.
[73] Lungu A, Cernencu AI, Vlasceanu GM, Florea NM, Ionita M, Iovu H. 3D POSS cages decorated 2D graphenic sheets: a versatile platform for silicon-carbonaceous nano-additives design. Compos B Eng 2021;207:108578.